The Meteoritical Society

Meteoritics & Planetary Science 1–14 (2024)
doi: 10.1111/maps.14255

Raman spectroscopy analysis of artificial space weathering effects of NWA 10580 CO3 meteorite

Ákos KERESZTURI[1,2], Sándor BIRI[3], Ildikó GYOLLAI[2,4]*, Zoltán JUHÁSZ[3], Csilla KIRÁLY[2,6], Richárd RÁCZ[3], Dániel REZES[1,2,5], Béla SULIK[3], Máté SZABÓ[2,4], Zoltán SZALAI[2,6,7], Péter SZÁVAI[2,6], and Tamás SZKLENÁR[1,2]

[1]Konkoly Thege Astronomical Institute, HUN-REN Research Centre for Astronomy and Earth Sciences, Budapest, Hungary
[2]CSFK, MTA Centre of Excellence, Budapest, Hungary
[3]HUN-REN Institute for Nuclear Research, Debrecen, Hungary
[4]Institute for Geological and Geochemical Research, HUN-REN Research Centre for Astronomy and Earth Sciences, Budapest, Hungary
[5]ELTE, Eotvos Lorand University of Sciences, Budapest, Hungary
[6]Geographical Institute, HUN-REN Research Centre for Astronomy and Earth Sciences, Budapest, Hungary
[7]Department of Environmental and Landscape Geography, ELTE, Eötvös Loránd University, Budapest, Hungary

***Correspondence**
Ildikó Gyollai, CSFK, MTA Centre of Excellence, Konkoly Thege Miklós út 15-17, Budapest H-1121, Hungary.
Email: gyollai.ildiko@csfk.org

(Received 11 August 2023; revision accepted 05 August 2024)

Abstract–A medium-grade, poorly weathered CO3-type meteorite was subjected to artificial space weathering by 1 keV protons in three subsequent steps, with gradually increasing doses from 10^{11} to 10^{17} protons per cm^2. The resulting mineral modifications were identified by Raman spectroscopy, with specific emphasis on main minerals such as olivine (bands: 817, 845 cm^{-1}), pyroxene (1007 cm^{-1}), and partly amorphous feldspar (509 cm^{-1}), considering variation in band shift and bandwidth (full width at half maximum, FWHM). After the first and second irradiations, variable band position changes were observed, probably from metastable alterations by Mg loss of the minerals, while the third stronger irradiation showed band shift dominated by amorphization. The olivine and pyroxene show weak increase in FWHM after the first irradiation, while more changes happened after the second and third irradiations. The flux after the third irradiation was higher than in other works, caused stronger damage in crystal lattice, partly resembling to dimerization as described by shock metamorphism. The glassy feldspar was characterized by high FWHM values already at the beginning, indicating weak crystallinity already that become even less crystallized, thus their bands disappeared after the third irradiation. Bands of hydrous minerals (goethite clay, chlorite) were not visible after the third irradiation, confirming some earlier results in the literature. Based on our results, moderately fresh surfaces could show stochastic but small spectral differences compared to the fresh most meteorites by metastable mineral alterations. The interpretation of Raman spectra of heavily space-weathered surfaces could further benefit from the joint evaluation of alteration induced by both shock impact alteration and space weathering.

INTRODUCTION

Linking meteorites to potential source asteroids is usually based on spectral similarity between them, however, while meteorites present feature-rich spectra, asteroid surface spectra are feature poor in general (Szalay et al., 2018). This situation arises from the fact that while meteorites are mainly fragments of intact asteroid interiors, asteroid surfaces are heavily space weathered (Chapman, 2004). Space weathering was studied on the

Hayabusa samples (Kayama et al., 2011a, 2011b, Kayama et al., 2013) also, including further recent works of Kereszturi et al. (2014) and Gucsik et al. (2017, 2020). To see the consequences of space weathering, artificial irradiation was applied on an average primitive meteorite and the results were analyzed mainly by Raman method. Such space weathering simulating proton irradiation was performed on the NWA 10580 meteorite, as being a frequently occurring and poorly altered types, thus representative to general for several meteorites. Although there were several recent findings in linking meteorite spectra to asteroid spectra (DeMeo et al., 2022; Krämer Ruggiu et al., 2021), there are still many poorly known aspects, which could be party explained by the better understanding of artificial irradiation induced mineral changes. Space weathering is a complex process (Brunetto et al., 2015), composed of galactic and solar energetic particles (cause implantation and sputtering), as well as UV irradiation, impacts processes (including small-scale and frequent micrometeorite bombardment called meteoritic gardening) and daily temperature fluctuations.

Range of information on space weathering comes from the Moon (Hapke, 2001; Keller & McKay, 1993, 1997), where the role of nanophase iron has been demonstrated (Pieters & Noble, 2016). Recently, asteroid sample return missions provided further materials to better understand space weathering (Matsumoto et al., 2015; Noguchi et al., 2011), also evaluating the role of nanophase iron, oxidation states (Thompson et al., 2016), and amorphous/Si enrichment (Matsumoto et al., 2016). In space weathering the target darkens and reddens (Kanuchova et al., 2015) besides the reduction of the strength and number of spectral bands. To better understand the consequences of the particle irradiation component of space weathering, artificial irradiation can be simulated by protons (Biri et al., 2012). For impact simulation, laser-induced heating has also been used to mimic the consequences of microscopic scale impacts (Ferus, 2020; Ferus et al., 2020), and ultraviolet irradiation tests have also been performed to better understand cosmic weathering (Hapke, 2001).

Review of Current Knowledge

A number of published works have reported on the effects of irradiation on organic materials, and in a few cases on meteoric main minerals. Brunetto et al. (2014) observed disordering of carbonaceous material in the irradiated Allende meteorite. Strazzulla and Brunetto (2017) performed irradiation experiment on Allende meteorite with He^+ ions using flux of 3×10^{16} ions per cm^2, which is similar to our third irradiation (10^{17} ions per cm^2) considering its range. They observed amorphization of olivine in Raman spectra dehydrogenation and amorphization of organic material. Baratta (2010) and Han et al. (2003) identified complete amorphization of graphite in Raman spectra on higher fluences in meteorites. Weber et al. (2023) have not observed change in peak positions using Raman spectra, but found an increase in fluorescence background in plagioclase-rich samples. Jakubek et al. (2022) observed decreasing of full width at half maximum (FWHM) of G band with increasing thermal metamorphism for organic matter and not the minerals analyzed here. Matsuoka et al. (2016) observed graphitization of organic material with increasing laser energies of irradiation, which could be observed rather in IR than in Raman spectra. They concluded that irradiation related alteration of organic material occurred rather in sample surface.

Hoffmann et al. (2019) performed Raman mapping on shocked howardite and observed inhomogeneity of shock alteration, which partly resembles to irradiation influenced alteration of minerals. Lantz et al. (2017) also noticed the amorphization of the silicates as seen in the Lance meteorite sample: the olivine doublet bands at about 850 and 820 cm^{-1} almost disappeared after irradiation in the Raman spectrum, which arises from coupled symmetric and asymmetric stretching vibrational modes of the SiO_4 tetrahedra (Kuebler et al., 2006). These modes could be efficiently observed under Raman with an olivine crystalline structure. The spectral shift of the IR and Raman bands could be due to the loss of magnesium by preferential sputtering of the lighter Mg to relative to Fe (Hapke et al., 1975) leading toward amorphization (Brucato et al., 2004; Demyk et al., 2004). In the Epinal meteorite, irradiated by 60 keV Ar^+ with fluences up 5×10^{16} ions cm^{-2}, Raman bands at 918, 855, and 825 cm^{-1} from olivine were observed, implying that the Fe content is lower than 6% using Raman spectra (Strazzulla et al., 2005). Values lower than 10% are typical for forsterite crystals, which imply the decrease in Fe content was due to irradiation. Lantz et al. (2015, 2017) studied Raman spectra olivine in Tagish Lake, Murchison and Lance meteorites, they found the weakening of major doublet at 820 and 850 cm^{-1} at high fluences. Brunetto et al. (2014) observed not only the disappearance of major doublet of olivine in Allende meteorite, but also the merging to a single band at 1040 cm^{-1}.

In order to investigate these questions, we undertook a study of proton irradiation on the NWA 10580 (CO3) meteorite to understand the consequences on mineral alteration and observability using Raman laboratory methods.

METHODS

The prepared sample had size of $4 \times 3 \times 1.5$ mm, it was cut to a roughly smooth plane surface but was not polished. No evident sign of Earth-based alteration could

be identified in the sample. This is a poorly altered primitive meteorite with a moderately unweathered material, mainly composed of forsterite, enstatite, and diopside, with many small chondrules, very few calcium–aluminum-rich inclusions (CAIs), sulfide blebs, all embedded in a fine-grained matrix. The morphology shows the typical Ornans-type (CO) carbonaceous chondritic texture with small chondrules and many refractory inclusions (Itoh & Tomeoka, 1989; Zhu et al., 2019). Approximately half of the sample volume is composed of a roughly homogeneous matrix material. The largest observed chondrule is sized around 250–300 μm diameter, which seems to be a porphyritic chondrule. The lithic fragments contain just a few accessory minerals (e.g., troilite and FeNi) besides the main constituent mineral phases.

The sample was analyzed before and after each irradiation actions with Raman spectrometer, targeting the same locations to allow recording the modifications of the same minerals. The locations for analysis were identified using the optical microscopic image of the Raman instrument indicated below (marked with codes like R1/2, R1/11, etc.). Locations were marked with letter plus number codes, the sample was subdivided by a grid system where codes like A2, B2, and C3 mark specific cells, while a further number marks the number of measuring location in the given cell, like A1/1 and A1/2, see for further details the table captions of Supporting information. During the measurements moderately small changes in the band position and FWHM values were measured, which were real and relevant values as based on the measurements of many different minerals in the sample, which presented resemble trends regarding of changes.

The used scanning electron microscope was a JEOL JSM-IT700 HR, using 20 keV voltage, 6 nA beam current, 40s point, and 100 s areal integration time. Three SEM images based examples on the morphology of the meteorite's texture can be seen in Figure 1 with the following features: 1—porphyritic chondrule, 2—Ba-rich secondary mineral, 3—fracture, 4—fine-grained matrix, 5—somewhat weathered unit of the meteorite, 6—coarse-grained matrix, 7—large olivine crystal, 8—troilite grain. Based on SEM measurements of around four dozen specific locations homogeneously arranged in the sample, these presented olivine of Fo75.2 ± 6.8 Fa24.8 ± 6.8 (n = 19), pyroxene: En34.5 ± 1.6 Wo20.4 ± 19.5 Fs45.1 ± 18.2 (n = 13), and small grain size (around 1 μm) anorthite were identified. Anorthite as a feldspar was present in the matrix and chondrule glass, similar to some other primitive chondrites (Grossman & Brearley, 2010; Huss et al., 2006). Accessories of troilite and FeNi metal phases also emerged. As a secondary phase, Ba containing barite probably formed by desert weathering on the Earth. The composition of the

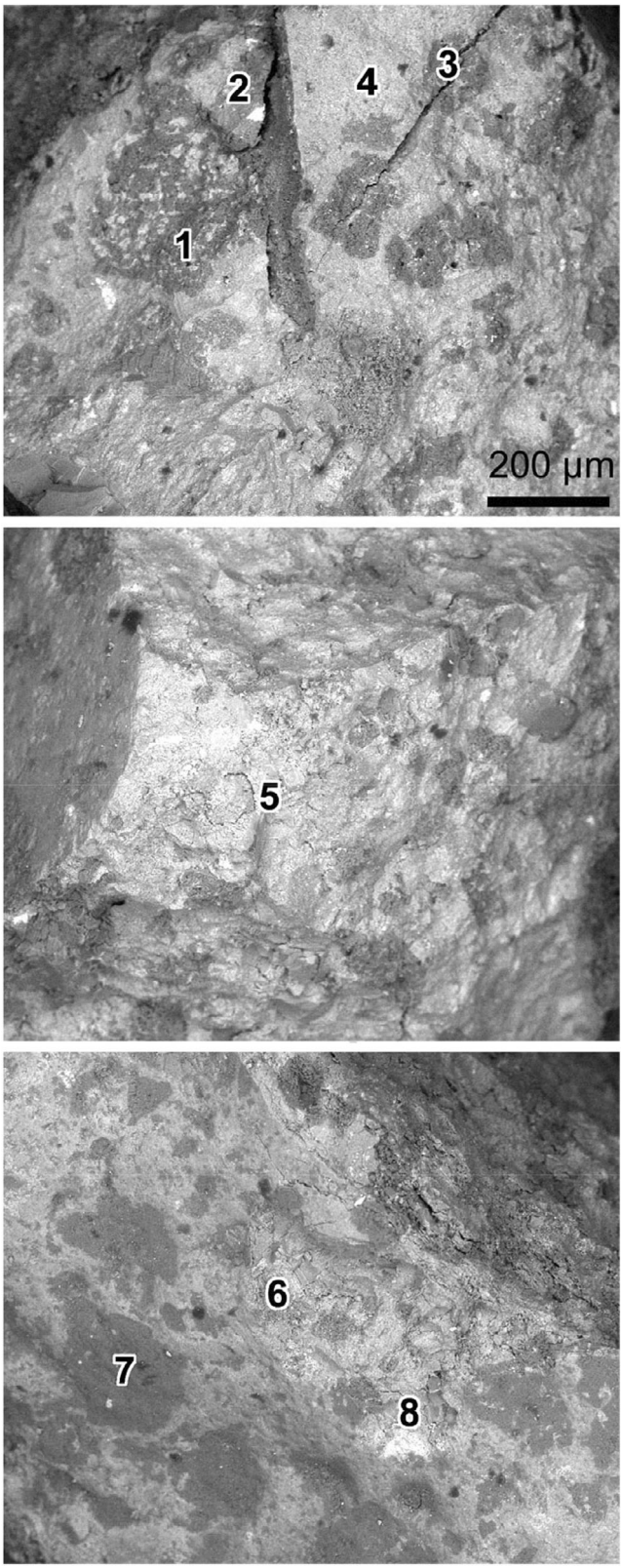

FIGURE 1. Example SEM images on the morphology of the analyzed sample. For the numbers refer to the main text.

analyzed sample agrees with those are characteristic to the CO3 chondrites in general (Bouvier et al., 2017). Changes on SEM images by irradiations could not be searched for as recording of SEM images would have required coating and decoating of the sample with amorphous carbon layer, what would have influenced the interpretation much.

The NWA 10580 CO3 sample was irradiated by 1 keV protons produced by the ECR ion source at ATOMKI (Biri et al., 2012) under vacuum conditions for three times: 15 sec (10^{11} ion cm^{-2}) for the first irradiation, for 1 h (10^{14} ion cm^{-2}) for the second irradiation, and for 1 day (10^{17} ion cm^{-2}) for the third irradiation. Observations of Ulysses and ACE satellites provided solar wind energies that showed the largest number of protons have around 1 keV energy (Gloeckler, 2003), thus we applied the particle bombardment using the most frequent ion type (proton) at the most frequent energy value (1 keV). The highest used fluence is roughly relevant to around 10–50 million years exposure duration, but only as a rough average estimation, because of CME-s, the total dose might differ. Note the earlier values are fluence values, thus represent the total number of bombarding protons by 1 cm^2 of the sample during the irradiation actions. When first, second, and third irradiations are mentioned in this work, these actions represent cumulative irradiation events, thus at the second irradiation event, the sample already have received the input from the first irradiation, and at the third, the sample already contained the input have received from the first and second together, though these three irradiation actions differed at 1000 times.

Raman spectroscopy was applied to determine the mineralogical characteristics. In a crystalline lattice, excitation features emerge as phonons by the periodic, elastic atomic arrangement, what produce vibrations in Raman spectra. Normal modes present observable wavelengths or frequencies, where phonons have a nonzero frequency connected to the Brillouin zone (primitive cell in reciprocal space) resulting in detectable spectral features. The Raman spectra was recorded by Morphologi G3-ID instrument produced by Malvern Instruments (Garzanti et al., 2015) and by Kaiser Optical Systems, Inc. Raman Rxn1 Spectrometer with NIR Laser Diode at 785 nm wavelength, using exposure time of 30 s at 10 mW laser power between 150 and 1150 cm^{-1}, while the size of the laser spot was 3 μm at 50× magnification. The spectral resolution was 1 cm^{-1} and the focal depth 1.82 μm. For the identification of Raman spectra, Bio-Rad's KnowItAll ID Expert software and the Morphologi software were used. Comparative spectra of the minerals were imported from the RUFF database by Lafuente et al. (2015).

Irradiation related changes in Raman spectra were studied by Brunetto et al. (2014), Strazzulla and Brunetto (2017), and Weber et al. (2022), which were used as references in our work. The positive band shift occurs mostly in shock-induced deformations, which were observed in our spectra as will be demonstrated later. Hence, shock metamorphic literature was also used in our work for the identification of Raman spectral features, using data from Van de Moortèle et al. (2007) (for olivine) and Durben et al. (1993) (for pyroxene). Before the irradiations, there were already differences in band positions because of compositional variations (e.g., higher original Mg content shows higher band position for the major doublet of olivine)—however, the trends after the irradiations were observable (see later), which influenced the minerals in a similar manner despite their original compositional differences. Results of Raman analysis should be carefully evaluated in the sense that energic laser shots might also modify the target mineral (see the corresponding part around the end of Discussion section). What substantially decreased the chance of influencing the sample by the used laser energy is the fact that all of the measurements were done manually, for example, the operator realized each measurement one by one, carefully adjusting the used energy for the given mineral with starting from the lowest used energy until to receive useful signal.

It is important to separate any possible modification of the sample by the irradiation test and the laser shots used during the Raman analysis. Consequences of Raman laser usage on meteorite minerals were reviewed by Morishita et al. (2011), indicating that sensitive carbonaceous material in meteorites might be modified; however, in this work, less-sensitive magmatic minerals were mostly surveyed (olivine, pyroxene, feldspar), which are more stable against low-energy laser-induced melting. According to Morishita et al. (2011), the Raman signal is influenced by laser power energy on the sample, laser excitation wavelength, and acquisition time, as well as described by Everall and Lumsdon (1991).

In this work a red laser was used, producing the available lowest energy range among various lasers for Raman analysis, and in all cases the energy was adjusted manually to the lowest possible that provides useful signal. Thus, although we cannot exclude the influence of Raman laser shots on mineral modification, but the irradiations (especially the third session) provided more energy to the sample than the laser itself, thus expected to have more impact on the alterations.

Before and after irradiations, the same areas were measured by Raman spectroscopy for comparison of changes and alteration of minerals. The accuracy of the targeting of measurements was better than 1 μm with high resolution, supported much by the comparison with the previously recorded field of view using the same instrument, what guarantees that each data series represent the same location. The first and second irradiations happened with roughly around the range of

TABLE 1. Statistical calculations of band position and FWHM changes of minerals, the Raman shifts are indicated in cm^{-1}.

Irradiation			First irradiation		Second irradiation		Third irradiation	
Mineral	Band		Band shift	FWHM change	Band shift	FWHM change	Band shift	FWHM change
Olivine	816	Average	0	4	1	−4	1	2
		Min	−3	−11	−1	−11	−1	−9
		Max	1	13	3	9	4	9
		Median	1	9	2	−6	1	4
		Deviation	2	10	2	8	2	7
	846	Average	−9	−4	1	1	1	1
		Min	−17	−15	0	−1	−3	−4
		Max	−1	3	3	1	4	6
		Median	−8	−1	0	1	1	0
		Deviation	8	8	2	1	3	4
Pyroxene	1014	Average	−2	2	−1	3	5	−6
		Min	−4	−1	−3	−6	1	−11
		Max	2	7	3	11	8	4
		Median	−1	1	−2	4	6	−7
		Deviation	2	4	3	8	3	4
Feldspar-like phase	505	Average	19	−3	1	−4		
		Min	0	−6	−2	−11		
		Max	37	0	4	3		
		Median	19	−3	1	−4		
		Deviation	26	4	4	10		

Note: fp bands did not emerge after the third irradiation.

fluences like in other works (Brunetto et al., 2020; Lantz et al., 2015, 2017), but the third irradiation happened by higher fluence than in most of the references.

Also note that to give an exact presentation of changes, large number of numerical values is needed, including several tables (Table 1, Tables S2–S6), and some similar structured paragraphs in the main text to make the results unified and comparable, despite such texts are not easy to read. However, the presented data sets allow the comparison of further research works to our acquired data, to make the tests repeatable and useful for planning future asteroid mission detectors.

To make the text easier and readable, the large tables were presented as Supporting information and are only cited in the main text. Tables S1 and S2 give an overview of measuring locations with original band positions and FWHM values, while S2b, S3, S4, S5, S5a, and S5b contain irradiation produced changes. The moderately large number of values were implemented to the manuscript in order to provide typical values for next research projects.

RESULTS

Mineral Identification

The Raman bands were identified following RRUFF database (Lafuente et al., 2015) regarding nonirradiated minerals. The irradiation related changes in Raman spectra have been studied previously by Brunetto et al. (2014) and Strazzulla and Brunetto (2017), which were used as references in our work. The following bands were used to identify the targeted minerals: 505 cm^{-1} indicate feldspar like glassy phase, 1010 cm^{-1} for pyroxene, and 819 and 840 cm^{-1} for olivine. The band shifts and FWHM values are calculated for the major bands of minerals listed before (Tables S1–S4, Table 1). Table S1 shows the summary for the identification of minerals. The main minerals smoothly embedded in their original meteorite texture (mainly chondrules) are olivine, pyroxene, feldspar, magnetite, goethite, clays as native components, while calcite is Earth-based weathering product.

Modifications of the Raman Spectra by Irradiation

Key Minerals

In this section, the band position modifications and FWHM changes induced by the irradiations are presented for the main mineral components. The values listed next according to minerals are calculated averages; for more details, refer to Tables S5a–d. Altogether 57 locations were measured in 5 measuring areas of the NWA 10580 sample: olivine (7 measuring points), pyroxene (8 measuring points), feldspar (3 measuring points), and other minerals in smaller amount.

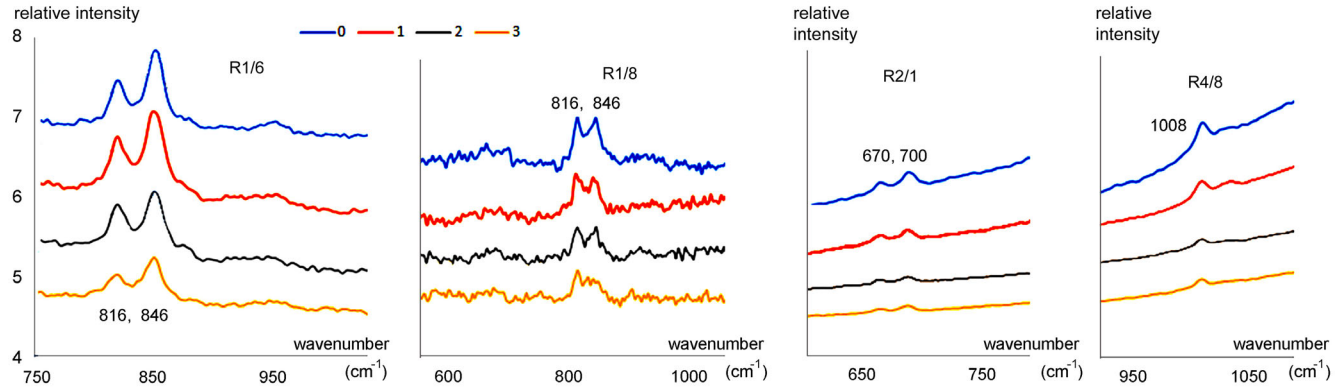

FIGURE 2. Example Raman spectra for irradiated sample positions (R1/6, 1/8, 2/1, 4/8) for before and after the first, second, and third irradiations (curves below each other).

Olivine

The band 853 cm^{-1} shows a negative band shift, whereas the band 817 cm^{-1} shows an increasing (positive) band shift after the first irradiation. The bands 817 and 853 cm^{-1} show increasing band shift (changing to 823 and 854 cm^{-1}) after the second and third irradiations (see Table 1). Regarding FWHM values of olivine, the following findings are relevant. The FWHM values of the 816 cm^{-1} band increased averagely +9 cm^{-1} after the first irradiation, −6 cm^{-1} after the second irradiation, while +4 cm^{-1} after the third irradiation (further specific values can be found in Table S1). The band 845 cm^{-1} has −4 cm^{-1} FWHM decrease after the first irradiation, +1 cm^{-1} after the second irradiation, and increased with +1 cm^{-1} after the third irradiation (further specific values can be found in Tables S2b and S5). During the first irradiation, the fluence was low, which could result in metastable alteration (Rietmeijer, 1991, 1999). After weak cosmic irradiation, the silicates (pyroxene, olivine) could be translated to metastable state due to the formation of Si-rich islands in the crystal structures, supported by the relocation of Fe-Mg cations in the crystal structure (Rietmeijer, 1991, 1999).

Pyroxene

Regarding band shifts, the band 1012 cm^{-1} of pyroxene shows negative band shift (decreasing wave number value) after the first and second irradiations, and increasing (positive) band shift after the third irradiation (Table 1). Regarding FWHM values of pyroxene, the following findings are relevant. The change of FWHM in band 1012 cm^{-1} is 2 cm^{-1} after the first and second irradiations. The change of FWHM is averagely +4 and −7 cm^{-1} after the third irradiation (further specific values can be found in Tables S3 and S5a–d).

Feldspar

Feldspar occurred as partly amorphous or glassy form with weak signals already at the beginning from very small grain size. This feldspar-like phase shows increasing band shift after the first and second irradiations; after the third irradiation, the band of feldspar disappear (at three different measurement locations). The band shift is averagely +19 cm^{-1} after the first irradiation. After the second irradiation, the band shift of feldspar is +1 cm^{-1} (Table 1). Regarding FWHM values in case of 468 cm^{-1}, the change is −6 cm^{-1} during transition to amorphous feldspar-like phase (505 cm^{-1}). After the first irradiation, the change of FWHM cannot be observed, but after the second irradiation FWHM change was averagely −4 cm^{-1} (Table S4). The irradiation defect of feldspar was studied by Kayama et al. (2011a, 2011b, 2013), they observed decrease in intensity and increase in FWHM value of the Raman band 505 cm^{-1} (vibration of SiO_4 rings), but in our measurements only the major band (505 cm^{-1}) was detected.

In summary, both the olivine (823 cm^{-1}) and the feldspar-like phase show increasing band shift after the first and second irradiations. The pyroxene and olivine show increasing band shift after the third irradiation, but the bands of feldspar disappear finally. The band shift of pyroxene shows negative values after the first and second irradiations, but change to positive trend after the third irradiation.

Figure 2 shows variation in major doublet (814, 846 cm^{-1} of olivine, R1, R6 locations), minor bands (670, 700 cm^{-1}, R2/1 location), and major band (1008 cm^{-1}, R8/1 location). In case of olivine, the measurement at R1/6 location shows decreasing intensity after the second and third irradiations. In case of R1/8 location, the band 846 cm^{-1} disappears after the third irradiation, only a shoulder can be observed there. In case of pyroxene, both of minor (670, 700 cm^{-1}) and major (1008 cm^{-1}) bands show decreasing intensity after the second and third irradiations. Figure 3 visualizes the average band position changes for different minerals. Changes on SEM images by irradiations could not be searched for as recording of SEM

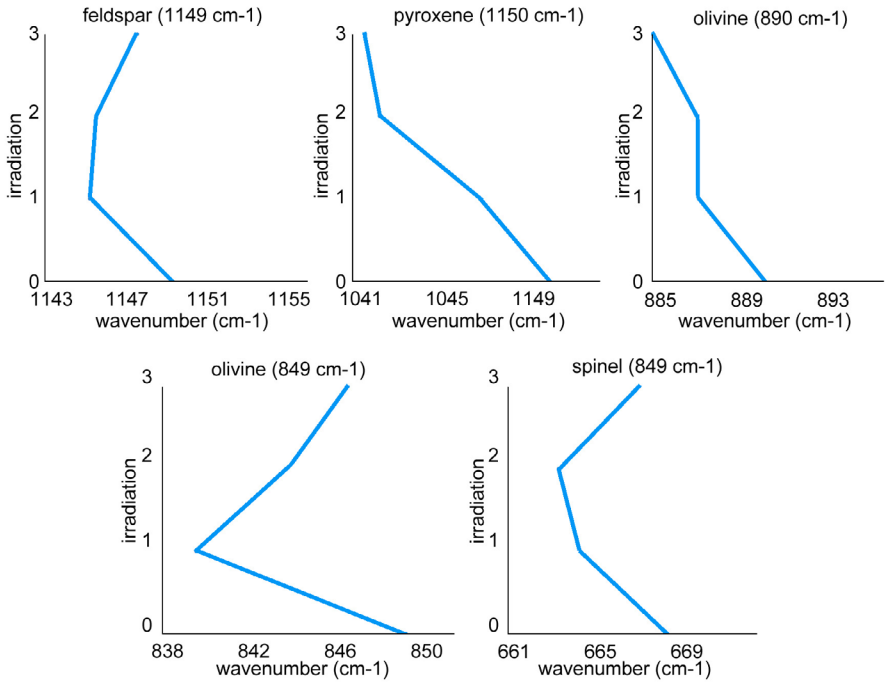

FIGURE 3. Band position changes (horizontal axis) at different irradiations (vertical axis) for the observed minerals (different diagrams).

images would have required coating and decoating of the sample with amorphous carbon layer, what would have influenced the interpretation much.

In summary, the FWHM shows an increase after the third irradiation in case of both of the major bands of olivine. The pyroxene shows an increase in FWHM after the first and second irradiations, but in case of the major doublet of olivine, any significant trend cannot be observed after the first and second irradiations. The band 505 cm^{-1} of partly amorphous feldspar shows decreasing FWHM disappeared after the first and second irradiations, and after the third irradiation, the bands of feldspar disappeared (see Table S6a for further values).

Auxiliary Minerals

Because of specifically interesting changes of phyllosilicates, their behavior is listed in this separate part. Phyllosilicate minerals occur altogether 19 times before irradiation, then of three cases after the first irradiation, and one case after second irradiation. After the third irradiation, the phyllosilicates were not detected, and their bands completely disappeared. Phyllosilicates as the elevated fluences might cause water loss after second and third irradiations, thus could be not detected (Tables S1 and S6b).

Magnetite, apatite, pyrite, marcasite, hematite, goethite, chromite, siderite, calcite, and chlorite bands appeared before and after the irradiations. Band disappearance after the irradiation observed in the case of hydrous mineral bands, like goethite (Table S6a,b). The weakening of the bands of these minerals were also observed after the irradiations.

The magnetite is an abundant phase, its band appeared 7 times before irradiation, 11 times after first irradiation, eight times after the second irradiation, and three times after the third irradiation. The goethite band appeared six times before irradiation, eight times after the first irradiation, nine times after the second irradiation, which disappeared everywhere after the third irradiation. Siderite band appeared mostly before irradiation (15 times), rarely after irradiations (one time after the first irradiation, three times after the second irradiation, and one time after the third irradiation; Table S6b).

Calcite band appears four times before and four times after the second irradiation, eight times after the first irradiation, and two times after the third irradiation. Chlorite band appeared four times before irradiation and two times after the first irradiation, then disappeared. After the third irradiation, bands of the hydrous minerals like clay, chlorite, goethite, and in most cases, the carbonates disappear.

Detailed numerical data and Raman spectral curves on the earlier observations can be found in the Supporting information, where various minor components can be seen in Data S1, with the following acronyms: cc, calcite; q,

quartz; fp gl, feldspar glass; chr, chromite; Mn-cc, manganese calcite; ap, apatite.

DISCUSSION

In the following, the interpretation of the observed changes are presented. The change in both FWHM and band positions are variable in the case of olivine (both band position increase and decrease can be observed), but this trend became consistent after the third irradiation, due to possible metastable change (movement Fe-Mg cations causing Mg-loss and Si-rich parts in crystal lattice) during the low irradiation (Rietmeijer, 2009). Similar low fluence was used in our first irradiation. It is worth comparing shock-driven and particle irradiation driven alterations of the mineral lattice. According to Durben et al. (1993), the positive band shift of olivine indicates dimer effects (polymerization of SiO_4 tetrahedra forming SiO_2 molecules) in metastable crystalline olivine. This positive band shift was observed after the second and third irradiations (+1 and +4 cm^{-1} averagely) in case of both bands of the major doublet. However, in our tests, after the irradiations mostly positive values were observed in band shift of 818 cm^{-1}, 60% (+1 cm^{-1}) after the first irradiation, 80% (+2 cm^{-1}) after the second irradiation, and 60% (+2.3 cm^{-1}) after the third irradiation (Table S2).

The band shift observed in this work increased by increasing fluences of irradiations, where positive band shift indicates amorphization of olivine. However, the band 845 cm^{-1} showed positive band shift in less cases: in 20% after the first (+9 cm^{-1}) and the second (+3 cm^{-1}) irradiations, and in 50% after the third irradiation (+2.5 cm^{-1}). Merging of major doublet of olivine was observed in case of one measuring area after the third irradiation. Increasing FWHM values after the third irradiation was observed in case of olivine (Tables S2a,b). The band shifts of olivine were caused by metastable alteration after the first (and partly second) irradiation where both positive and negative values were observed. After the third irradiation, both of FWHM and band shift values showed only positive trend, by the higher fluences.

In case of pyroxene, the FWHM of band 1014 cm^{-1} increases after the first and second irradiations, and shows a decrease after the third irradiation (Table S3). Band shift was negative after the first irradiation (−2.5 cm^{-1} in case of 60% of data), whereas after the second irradiation, 20% increased (+3 cm^{-1}) and 80% decreased (−2 cm^{-1}), but after third irradiation, all analyzed mineral locations were characterized by positive band shifts (all of data, averagely +5 cm^{-1}). The negative trend (decreasing values) shows Mg loss from the crystalline structure after the irradiation (Lantz et al., 2017); however, this change was identified by infrared and not Raman spectroscopy in their publication; thus, further work/analysis is needed to verify the connection with Raman measurements.

The feldspar is characterized by increasing band shift after the first and second irradiations, then its bands disappeared by further amorphization and decomposition after the third irradiation (Table S4). It has low-intensity bands with high FWHM values before the irradiation, indicating originally partly amorphous occurrence (Table S4). The feldspar might be not well crystallized originally, similar to the observations of Lewis and Jones (2016), who found feldspars in chondritic material recrystalize to amorphous, fine-grained component, thus presenting less intense bands with high FWHM, and its bands completely disappeared after the third irradiation was heavily amorphized by the higher fluence irradiation. This mineral phase was already poorly crystallized and very small grained for detailed analysis. The originally small grains could have transformed to several different products and amorphous components, thus could not be identified after the irradiation tests. According to Rietmeijer (1991), feldspars were already modified during the annealing history of chondritic amorphous material, also weakening the crystallized structure. According to the expectations, the less crystallized minerals (like partly amorphous feldspars, silica, hydrous minerals) are not stable for the used elevated fluences in agreement with Lantz et al. (2017) and Brunetto et al. (2020).

Such alteration starts in an amorphous rim during the bombardment of solar particles (Craig & Sears, 2011). Alternatively, amorphous feldspar could also be formed by thermal breakdown of high pressure, metastable polimorphs, like hollandite due to postshock annealing (Kubo et al., 2010, 2017), under specific proper conditions. In their experience, the hollandite has broken down to amorphous feldspar phase due to the electron beam. According to Alexander et al. (1989), the matrices of chondrites could be modified to amorphous–semi-amorphous feldspar-rich particles due to solar particle bombardment. Ewing et al. (2000) and Demyk et al. (2004) also discussed that minerals become amorphous after irradiation, and after strong irradiation, complete disappearance of their bands could be observed —just like in our case. Emergence of oxides or phyllosilicates along with the decrease in feldspar bands (as possible alteration products) at the targeted locations could not be observed.

The band shifts of Fe-Mg bearing minerals in general correspond to not only decomposition of their structure, but also variation in Fe-Mg composition. Negative band shift of Raman band indicates Mg loss causing Fe increase (Lantz et al., 2017). This feature can be observed in more of the measuring points of pyroxenes and olivines after the first and second irradiations. With increasing irradiation, the less

stable, water-bearing minerals' bands disappeared (17 of 19 phyllosilicates containing locations) after the first irradiation (Table S6b). The goethite bands disappear (two points of five occurrences after the second irradiation, Table S6b). After the third irradiation, all of the goethite bands, and after the second irradiation, all of the phyllosilicate bands disappear due to water loss in our measuring areas as already been mentioned in other works (e.g., Brunetto et al., 2020; Lantz et al., 2015, 2017).

Alteration by the Irradiations

After the aqueous alteration in the parent body, H_2O was implemented to the crystal lattice as iron oxides and carbonates (Neubeck et al., 2014) in general. During alteration by irradiation, decrease in band intensities can be observed in case of phyllosilicates (R1/2, R1/9, R1/12 locations). In more cases (70% of measurements), degradation (band disappearance) of clay minerals can be observed already after the first irradiation (R3/1, 3, 4, 8, 12; R4/2–5 locations). The OH loss is indicated by decreasing intensity of bands near 1600 and 3600 cm^{-1}. Following are the degradation of phyllosilicate minerals by water loss (indicated in Tables S1 and S6a): the phyllosilicate bands were present before irradiation (Table S6b) at 17 measurement locations, while only at two locations can be observed after the first irradiation, and disappeared after the second and third irradiations (phyllosilicates minerals can be observed before irradiation at following locations: R3/1, 2, 4, 8, 12; R4/2–5, 10, 12, 14–18, R1/2, 9,12; R2/7).

Along with the degradation of phyllosilicates after the first irradiation, emergence of olivine and hematite and goethite after the second irradiation (R3/1) could be observed (Figure S7). Similar alteration was observed by Fornaro et al. (2018) after their UV–irradiation experiment. The transformation of phyllosilicates to iron oxides (goethite, hematite) by chemical weathering, however, in soils and not by irradiation was also observed by Schwertmann (1988) previously.

Depending on the rate of water loss, phyllosilicate minerals can produce different type of iron oxides: Hematite occurred after the second irradiation (R1/2, R1/11 locations) along with the disappearance of phyllosilicate mineral bands, with the appearance of hematite band (407 cm^{-1}). The formation of goethite occurs after the second irradiation (R1/10, R3/8) (less water loss). Phyllosilicate minerals could be altered to magnetite after the first irradiation (R4/2, 3, 5, 6) due to complete water loss. This mineral alteration was observed but in soils due to weathering by Hyodo et al. (2020).

Disappearance of main mineral bands could be also observed. Feldspar bands disappeared due to amorphization probably after the third irradiation (three measuring areas – R2/6, a1/3, and a1/9 location). Chlorite and siderite disappear after the first irradiation (R1/5–6). The chlorite and siderite were weakly crystallized before the irradiation, hence could disappear after the first irradiation. It is possible and probable that phyllosilicates were modified by water loss and amorphization described by Lantz et al. (2017) due to water loss. The decomposition of carbonate occurs above 400°C, though here at small atomic scale bonds could be broken by the high-energy protons. However, it is worth mentioning that the confirmation of these alterations requires further analysis, not targeted in this work.

Weakening and disappearance of feldspar bands during the irradiation series indicates amorphization and weakening of crystalline lattice. Gleason et al. (2022) found that the amorphization by shock effect of plagioclase begins at 5 GPa and becomes a high-density amorphous phase at 32 ± 10 GPa, what partially recrystallized afterward, here resemble process might happened. In the Martian lherzolitic shergottite Grove Mountains (GRV) 99027, Wang and Chen (2006) observed plagioclase that experienced shock melting and recrystallization. Luu et al. (2021) irradiated albite and microcline with 3 MeV Si^{2+} to a maximum fluence of 2×10^{16} ions cm^{-2}, found that amorphization of feldspars, which is approximately two orders of magnitude higher fluence than in our experiment. Furthermore, alkali ions found to be important in the amorphization kinetics, and Moroz et al. (2014) irradiated Fe-poor plagioclase (andesine–labradorite) with nanosecond pulser laser (1.5×10^9 Jcm^{-2} s^{-1}, then 4×10^{10} Jcm^{-2} s^{-1} average energy flux) producing nano- and submicrometer Fe inclusion inside the layers. Zeng et al. (2021) investigated the solar wind-produced OH/H_2O in plagioclase (An50–53), 5 keV H^+ at fluence of $\sim 1 \times 10^{17}$ H^+/cm^2. Pure minerals are useful references also: Yang et al. (2016) studied alteration of olivine after laser irradiation caused two major spectral feature changes, the maximum FWHM of all Raman bands increased upon irradiations. Kayama et al. (2011b) did not observed any red emission of CL methods (in which reddening was observed by IR methods by Brunetto et al. (2006), Lantz et al. [2015, 2017]). Gucsik et al. (2017) detected no reddening in cathodoluminescence spectra, but they detected blue emission as deformation center in the shocked space-weathered Itokawa samples. Gucsik et al. (2020) observed decreased intensity of SiO_4 ring vibrations and increase in luminescence background of Raman spectra in the shocked, space-weathered bulk meteorites and Itokawa samples. In our work, upon irradiations all Raman modes experienced decreasing peak shift (downshift) by 4–6 cm^{-1} also. Under future tests, further irradiation actions with pure minerals (RRUFF database; Brunetto et al., 2014; Gucsik et al., 2020; Strazzulla & Brunetto, 2017; Weber et al., 2022) should be

also realized, however, this aspect was out of the possibilities in this work.

For the exclusion of the Raman laser-induced mineral changes, refer to the corresponding part of the Methods section. As a summary regarding alterations (mainly in S6a,b marked by yellow color), siderite might transform to goethite due to Fe loss (R2/9), similar to that observed by Liu et al. (2021). The clay bands disappeared (R3/1) due to water loss together with the emergence of goethite, hematite, and siderite. The origin of calcite is especially interesting as might formed on the Earth after the fall of the meteorite. It appears mostly after the first irradiation, and its band disappear after the third irradiation. Based on the published literature, calcite might form from carbonates by irradiation during depolymerization of SiO_4 tetrahedra, though this has been tested not by protons but neutrons (Zhang et al., 2023). Calcite formation could also happen in clay and amorphous carbonate mixtures (Rodriguez-Navarro et al., 2015). However, as mentioned earlier, the confirmation of these modifications requires further different tests. Pyrite and chromite bands emerge mostly after the third irradiation—however, the firm evaluation of these observations need further work with different observation strategy. According to Allard et al. (2012), the irradiation induced change of redox state of Fe in the structure could support various mineral alterations.

CONCLUSION

Artificial space weathering by 1 keV protons were performed on the NWA 10580 meteorite at three subsequent gradually increasing steps. Altogether 74 measuring locations were analyzed before and after the irradiations by Raman methods, focusing on olivine, pyroxene, and feldspar, regarding variations in band shift and FWHM values. Other minerals, like clay, apatite, pyrite, marcasite, goethite, hematite, chromite siderite, calcite, and chlorite, were also detected before and after the irradiations by occasionally including possible decomposition. The band from less crystallized feldspar and hydrous minerals (clay, chlorite, and goethite) disappeared after the third irradiation possible due to the water loss and decomposition. In several cases, the bands of less crystallized hydrous minerals disappeared already after the first irradiation. This observation indicates that the rarity or lack of hydrated phases on asteroid surfaces need not necessarily mark to exclude wet alteration rich interior below a shallow-weathered crust—what might be considered during the planning of the observations by next asteroid missions.

Evaluating the band shift of olivine, no significant trend could be observed at the major double after the first irradiation, and after second and third irradiations only minor increase (1 cm^{-1}) was present. For pyroxene, decreasing trend (−1 and −2 cm^{-1}) at the first and second irradiations can be observed in the average band shift values, while after the third irradiation a moderate increase in band shift (+5 cm^{-1}) could be observed. Although the shift values are small, they were parallelly identified at several locations. According to Lantz et al. (2017), the negative band shift of major bands of pyroxene and olivine was caused by Mg loss, what was supported by our tests. At even stronger irradiation (here after the third irradiation), both olivine (+1 cm^{-1}) and pyroxene (+6 cm^{-1}) showed increasing band shift due to amorphization. The feldspar showed moderate increase in band shift after the first irradiation, and minor change after the second irradiation, finally the feldspar band disappeared after the third irradiation probably by heavy amorphization.

The olivine and pyroxene show weak increase in FWHM after the first irradiation, and more changes happened after the second and third irradiations. The increase in FWHM was observed after the irradiation in case of organic carbons as described by Morishita et al. (2011), which is not about the same minerals analyzed here, however, is an interesting related work. The hydrous minerals (goethite clay, chlorite) were observed mostly before irradiation and after the first irradiation, in which bands decreased after the second irradiation, and completely disappeared after the third irradiation. These less stable Fe-bearing minerals might be altered to more stable minerals like hematite and magnetite after the irradiations.

The positive band shift after the third irradiation (together with the increase in FWHM values indicating amorphization) was identified in this research for most minerals, while in the works of Lantz et al. (2017) and Brunetto et al. (2020) they described only negative band shifts in cm^{-1} for Mg-bearing minerals, which was interpreted as Mg loss from crystal structure. The difference could be that we used higher fluence after the third irradiation than in other works, which caused stronger damage of the crystal lattice (dimerization as described by shock metamorphism in Johnson et al. 2003, 2007; Sharp & DeCarli, 2006; Van de Moortèle et al., 2007; Dyar et al., 2011; Gyollai et al., 2017).

In general, the three main minerals showed different average FWHM trends. The feldspar and pyroxene showed increasing FWHM after the first and second irradiations. For olivine, significant FWHM trend of the major doublet could not be observed after the first and second irradiations, but after the third irradiation a minor increase (+1 to +2 cm^{-1}) was present. After the first and second irradiations, minor increase can be seen in FWHM values (+2 and +3 cm^{-1} averagely) in case of pyroxenes too. The

feldspar was characterized by high FWHM values while it was observable, indicating weak crystallinity from the beginning.

Mineral changes could be also indicated some by observations from the irradiation. In general, the bands of hydrous minerals (phyllosilicate, chlorite, goethite) started to diminish, while other phases emerged after the first irradiation (including possible "alteration products" like hematite, magnetite), and all of their bands disappeared after the third irradiation. Thus, we straighten some earlier results (Brunetto et al., 2020; Lantz et al., 2017) on the water loss, and disappearance of water-bearing mineral bands. During the irradiations, the occurrence of Fe-bearing clay minerals decreased, and goethite and hematite emerged, while pyrite and chromite were also observed only after the third irradiation. Hematite and goethite could form from clay minerals by water loss in theory, what might have happened here, however could not firmly proved. The degradation of clay minerals due to Mg loss and water loss was observed by Lantz et al. (2015, 2017) and Brunetto et al. (2014, 2015), and here probably also the same happened—but the firm confirmation requires further analysis by more sophisticated observing strategy. Alteration of carbonates are not described by others after irradiations, while this feature was observed in our irradiated sample—however, here also further analysis is needed to gain firm results.

Acknowledgments—This project was supported by the K_138594 project of NKFIH. Juhasz Z. acknowledges the funding from the Bolyai Fellowship. This work was also supported in part by Europlanet 2024 RI which has received funding from the European Union's Horizon 2020 Research Innovation Programme under Grant Agreement No. 871149.

Data Availability Statement—The data that support the findings of this study are available from the corresponding author upon reasonable request.

Editorial Handling—Dr. Edward Anthony Cloutis

REFERENCES

Alexander, C. M. O'D., Hutchison, R., and Barber, D. J. 1989. Origin of Chondrule Rims and Interchondrule Matrices in Unequilibrated Ordinary Chondrites. *Earth and Planetary Science Letters* 95: 187–207.

Allard, T., Balan, E., Calas, G., Fourdrin, C., Morichon, E., and Sorieul, S. 2012. Radiation-Induced Defects in Clay Minerals: A Review. *Nuclear Instruments and Methods in Physics Research Section B: Beam Interactions with Materials and Atoms* 277: 112–120.

Baratta, G. A. 2010. In-Situ Studies of Ion Irradiated Materials Relevant to Planetary Science *European Planetary Science Congress, p. 249*.

Biri, S., Rácz, R., and Pálinkás, J. 2012. Status and Special Features of the Atomki ECR Ion Source. *Review of Scientific Instruments* 83: 02A341.

Bouvier, A., Gattacceca, J., Grossman, J., and Metzler, K. 2017. The Meteoritical Bulletin No. 105. *Meteoritics & Planetary Science* 52: 2411.

Brucato, J. R., Strazzulla, G., Baratta, G., and Colangeli, L. 2004. Forsterite Amorphisation by Ion Irradiation: Monitoring by Infrared Spectroscopy. *Astronomy & Astrophysics* 413: 395–401.

Brunetto, R., Lantz, C., Ledu, D., Baklouti, D., Barucci, M. A., Beck, P., et al. 2014. Ion Irradiation of Allende Meteorite Probed by Visible, IR, and Raman Spectroscopies. *Icarus* 237: 278–292.

Brunetto, R., Lantz, C., Nakamura, T., Baklouti, D., Le Pivert-Jolivet, T., Kobayashi, S., and Borondics, F. 2020. Characterizing Irradiated Surfaces Using IR Spectroscopy. *Icarus* 345: 113722.

Brunetto, R., Loeffler, M. J., Nesvorný, D., Sasaki, S., and Strazzulla, G. 2015. Asteroid Surface Alteration by Space Weathering Processes. In *Asteroids IV*, edited by P. Michel, F. E. DeMeo, and W. F. Bottke. Tucson: University of Arizona Press.

Brunetto, R., Vernazza, P., Marchi, S., Birlan, M., Fulchignoni, M., Orofino, V., and Strazzulla, G. 2006. Modeling Asteroid Surfaces From Observations and Irradiation Experiments: The Case of 832 Karin. *Icarus* 184: 327–337.

Chapman, C. R. 2004. Space Weathering of Asteroid Surfaces. *Annual Review of Earth and Planetary Sciences* 32: 539–567.

Craig, J. P., and Sears, D. W. 2011. Thermoluminescence as a Technique for Determining the Nature and History of Small Solar System Particles. *Geochronometria* 38: 272–281.

DeMeo, F. E., Burt, B. J., Marsset, M., Polishook, D., Burbine, T. H., Carry, B., et al. 2022. Connecting Asteroids and Meteorites with Visible and near-Infrared Spectroscopy. *Icarus* 380: 114971.

Demyk, K., d'Hendecourt, L., Leroux, H., Jones, A. P., and Borg, J. 2004. IR Spectroscopic Study of Olivine, Enstatite and Diopside Irradiated with Low Energy H and He Ions. *Astronomy & Astrophysics* 420: 233–243.

Durben, D. J., McMillan, P. F., and Wolf, G. H. 1993. Raman Study of the High-Pressure Behavior of Forsterite (Mg_2SiO_4) Crystal and Glass. *American Mineralogist* 78: 1143–48.

Dyar, M. D., Glotch, T. D., Lane, M. D., Wopenka, B., Tucker, J. M., Seaman, S. J., Marchand, G. J., et al. 2011. Spectroscopy of Yamato 984028. *Polar Science* 4: 530–549.

Everall, N. J., and Lumsdon, J. 1991. The Effect of Laser-Induced Heating upon the Vibrational Raman Spectra of Graphites and Carbon Fibers. *Carbon* 29: 133–37.

Ewing, R. C., Meldrum, A., Wang, L., and Wang, S. 2000. Radiation-Induced Amorphization. *Reviews in Mineralogy and Geochemistry* 39: 319–361.

Ferus, M. 2020. In *Proceedings of the International Meteor Conference*, edited by U. Pajer, J. Rendtel, M. Gyssens, and C. Verbeeck, 47–54. Bollmannsruh, Germany: International Meteor Organization.

Ferus, M., Petera, L., Koukal, J., Lenža, L., Drtinova, B., Haloda, J., Matýsek, D., et al. 2020. Elemental composition, mineralogy and orbital parameters of the Porangaba meteorite. *Icarus* 341: 113670.

Fornaro, T., Boosman, A., Brucato, J. R., ten Kate, I. L., Siljeström, S., Poggiali, G., Steele, A., et al. 2018. UV Irradiation of Biomarkers Adsorbed on Minerals under Martian-Like Conditions: Hints for Life Detection on Mars. *Icarus* 313: 38–60.

Garzanti, E., Resentini, A., Andò, S., Vezzoli, G., Pereira, A., and Vermeesch, P. 2015. Physical Controls on Sand Composition and Relative Durability of Detrital Minerals during Ultra-Long Distance Littoral and Aeolian Transport (Namibia and Southern Angola). *Sedimentology* 62: 971–996.

Gleason, A. E., Park, S., Rittman, D. R., Ravasio, A., Langenhorst, F., Bolis, R. M., Granados, E., et al. 2022. Ultrafast Structural Response of Shock-Compressed Plagioclase. *Meteoritics & Planetary Science* 57: 635–643.

Gloeckler, G. 2003. Ubiquitous Suprathermal Tails on the Solar Wind and Pickup Ion Distributions. Solar Wind 10, Proceedings CP679 https://doi.org/10.1063/1.1618663.

Grossman, J. N., and Brearley, A. J. 2010. The Onset of Metamorphism in Ordinary and Carbonaceous Chondrites. *Meteoritics & Planetary Science* 58: 87–122.

Gucsik, A., Futó, P., Simonia, I., Vanyó, J., and Csámer, Á. 2020. Space Weathering-Related Evolution of Fine-Grained Asteroidal and Cometary Materials: An Implication for the Sample Return Planetary Missions (H-Space 2020, Budapest).

Gucsik, A., Nakamura, T., Jäger, C., Ninagawa, K., Nishido, H., Kayama, M., Tsuchiyama, A., Ott, U., and Kereszturi, Á. 2017. Luminescence Spectroscopical Properties of Plagioclase Particles from the Hayabusa Sample Return Mission: An Implication for Study of Space Weathering Processes in the Asteroid Itokawa. *Microscopy and Microanalysis* 23: 179–186.

Gyollai, I., Kereszturi, Á., Szabó, M., Chatzitheodoridis, E., and Berczi, S. Z. 2017. Másodlagos ásványok keletkezési viszonyainak vizsgálata a Nakhla, Yamato, Lafayette és Governador Valadares marsi meteoritokban. In *A talajtakaró geonómiája, 289*, 262–69. Budapest, Hungary: ELTE.

Han, K.-H., Spemann, D., Esquinazi, P., Höhne, R., Riede, V., and Butz, T. 2003. Ferromagnetic Spots in Graphite Produced by Proton Irradiation. *Advanced Materials* 15: 1719–22.

Hapke, B. 2001. Space Weathering from Mercury to the Asteroid Belt. *Journal of Geophysical Research: Planets* 106(E5): 10039–73.

Hapke, B., Cassidy, W., and Wells, E. 1975. Effects of Vapor-Phase Deposition Processes on the Optical, Chemical, and Magnetic Properties OE the Lunar Regolith. *The Moon* 13: 339–353.

Hoffmann, V. H., Wimmer, K., Hochleitner, R., Kaliwoda, M., and Uysal, I. 2019. Magnetic Classification and Shock Stage (on Plagioclase by Raman Spectroscopy) of the Saricicek Meteorite (Howardite) 82nd Annual Meeting of the Meteoritical Society, vol. 82, p. 6449.

Huss, G. R., Rubin, A. E., and Grossman, J. N. 2006. Thermal Metamorphism in Chondrites. In *Meteorites and the Early Solar System II*, edited by D. S. Lauretta, and H. Y. McSween, Jr., vol. 943, 567–586. Tucson: University of Arizona Press.

Hyodo, M., Sano, T., Matsumoto, M., Seto, Y., Bradák, B., Suzuki, K., Fukuda, J., et al. 2020. Nanosized Authigenic Magnetite and Hematite Particles in Mature-Paleosol Phyllosilicates: New Evidence for a Magnetic Enhancement Mechanism in Loess Sequences of China. *Journal of Geophysical Research: Solid Earth* 125: e2019JB018705.

Itoh, D., and Tomeoka, K. 1989. Na-Bearing Ca-Al-Rich Inclusions in Four CO3 Chondrites, Kainsaz, Ornans, Lance, and Warrenton. In *Antarctic Meteorites XXIII. Papers Presented to the 23rd Symposium on Antarctic Meteorites*, 42–44. Tokyo, Japan: NIPR.

Jakubek, R. S., Righter, K., and Fries, M. D. 2022. Raman Spectroscopic Characterization of Petrologic Type in Chondrite Chips and Thin Sections and Potential Applications for Meteorite Pairing *53rd Lunar and Planetary Science Conference*, abstract #2678, p. 1095.

Johnson, J. R., Hörz, F., and Staid, M. I. 2003. Thermal Infrared Spectroscopy and Modeling of Experimentally Shocked Plagioclase Feldspars. *American Mineralogist* 88: 1575–82.

Johnson, J. R., Staid, M. I., and Kraft, M. D. 2007. Thermal Infrared Spectroscopy and Modeling of Experimentally Shocked Basalts. *American Mineralogist* 92: 1148–57.

Kanuchova, Z., Brunetto, R., Fulvio, D., and Strazzulla, G. 2015. Near-Ultraviolet Bluing after Space Weathering of Silicates and Meteorites. *Icarus* 258: 289–296.

Kayama, M., Nishido, H., Toyoda, S., Komuro, K., Finch, A. A., Lee, M. R., and Ninagawa, K. 2013. He+ Ion Implantation and Electron Irradiation Effects on Cathodoluminescence of Plagioclase. *Physics and Chemistry of Minerals* 40: 531–545.

Kayama, M., Nishido, H., Toyoda, S., Komuro, K., and Ninagawa, K. 2011a. Radiation Effects on Cathodoluminescence of Albite. *American Mineralogist* 96: 1238–47.

Kayama, M., Nishido, H., Toyoda, S., Komuro, K., and Ninagawa, K. 2011b. Combined Cathodoluminescence and Micro-Raman Study of Helium-Ion-Implanted Albite. *Spectroscopy Letters* 44: 526–29.

Keller, L. P., and McKay, D. S. 1993. Discovery of Vapor Deposits in the Lunar Regolith. *Science* 261: 1305–7.

Keller, L. P., and McKay, D. S. 1997. The Nature and Origin of Rims on Lunar Soil Grains. *Geochimica et Cosmochimica Acta* 61: 2331–41.

Kereszturi, A., Gucsik, A., Nakamura, T., Nishido, H., Ninagawa, K., and Kayama, M. 2014. Impacts on Airless Objects under Microgravity and Possible Related Structures in Itokawa Asteroid Sample. *International Journal of Condensed Matter, Advanced Materials, and Superconductivity Research* 13: 21. Horizons in World Physics, Volume 282, July 1, 2014, pp. 21–39.

Krämer Ruggiu, L., Beck, P., Gattacceca, J., and Eschrig, J. 2021. Visible-Infrared Spectroscopy of Ungrouped and Rare Meteorites Brings Further Constraints on Meteorite-Asteroid Connections. *Icarus* 362: 114393.

Kubo, T., Kimura, M., Kato, T., Nishi, M., Tominaga, A., Kikegawa, T., and Funakoshi, K. I. 2010. Plagioclase Breakdown as an Indicator for Shock Conditions of Meteorites. *Nature Geoscience* 3: 41–45.

Kubo, T., Kono, M., Imamura, M., Kato, T., Uehara, S., Kondo, T., Higo, Y., Tange, Y., and Kikegawa, T. 2017. Formation of a Metastable Hollandite Phase from Amorphous Plagioclase: A Possible Origin of Lingunite in Shocked Chondritic Meteorites. *Physics of the Earth and Planetary Interiors* 272: 50–57.

Kuebler, K. E., Jolliff, B. L., Wang, A., and Haskin, L. A. 2006. Extracting Olivine (Fo–Fa) Compositions from

Raman Spectral Peak Positions. *Geochimica et Cosmochimica Acta* 70: 6201–22.

Lafuente, B., Downs, R. T., Yang, H., and Stone, N. 2015. The Power of Databases: the RRUFF Project. In *Highlights in Mineralogical Crystallography*, edited by T. Armbruster, and R. M. Danisi, 1–30. Berlin, Germany: De Gruyter.

Lantz, C., Brunetto, R., Barucci, M. A., Dartois, E., Duprat, J., Engrand, C., Godard, M., et al. 2015. Ion Irradiation of the Murchison Meteorite: Visible to Mid-Infrared Spectroscopic Results. *Astronomy & Astrophysics* 577: A41.

Lantz, C., Brunetto, R., Barucci, M. A., Fornasier, S., Baklouti, D., Bourçois, J., and Godard, M. 2017. Ion Irradiation of Carbonaceous Chondrites: A New View of Space Weathering on Primitive Asteroids. *Icarus* 285: 43–57.

Lewis, J. A., and Jones, R. H. 2016. Phosphate and Feldspar Mineralogy of Equilibrated L Chondrites: The Record of Metasomatism During Metamorphism in Ordinary Chondrite Parent Bodies. *Meteoritics & Planetary Science* 51: 1886–1913.

Liu, J. C., He, H. P., Michalski, J., Cuadros, J., Yao, Y. Z., Tan, W., Qin, X. R., Li, S. Y., and Wei, G. J. 2021. Reflectance Spectroscopy Applied to Clay Mineralogy and Alteration Intensity of a Thick Basaltic Weathering Sequence in Hainan Island, South China. *Applied Clay Science* 201: 105923.

Luu, V. N., Murakami, K., Samouh, H., Maruyama, I., Ohkubo, T., Tom, P. P., Chen, L., et al. 2021. Changes in Properties of Alpha-Quartz and Feldspars under 3 MeV Si-Ion Irradiation. *Journal of Nuclear Materials* 545: 152734.

Matsumoto, T., Tsuchiyama, A., Miyake, A., Noguchi, T., Nakamura, M., Uesugi, K., Takeuchi, A., Suzuki, Y., and Nakano, T. 2015. Surface and Internal Structures of a Space-Weathered Rim of an Itokawa Regolith Particle. *Icarus* 257: 230–38.

Matsumoto, T., Tsuchiyama, A., Uesugi, K., Nakano, T., Uesugi, M., Matsuno, J., et al. 2016. Nanomorphology of Itokawa Regolith Particles: Application to Space-Weathering Processes Affecting the Itokawa Asteroid. *Geochimica et Cosmochimica Acta* 187: 195–217.

Matsuoka, M., Nakamura, T., Kimura, Y., Hiroi, T., Nakamura, R., Okumura, S., and Sasaki, S. 2016, March. Reproducing Space Weathering on C-Type Asteroids with Low-Energy Laser Irradiation Experiments of the Murchison Meteorite *47th Lunar and Planetary Science Conference*, abstract #1903, p. 1823.

Morishita, K., Nara, M., Amari, S., and Matsuda, J. 2011. On the Effect of Laser-Induced Heating in a Raman Spectroscopic Study of Carbonaceous Material in Meteorite. *Spectroscopy Letters* 44: 459–463.

Moroz, L. V., Starukhina, L. V., Rout, S. S., Sasaki, S., Helbert, J., Baither, D., Bischoff, A., and Hiesinger, H. 2014. Space Weathering of Silicate Regoliths with Various FeO Contents: New Insights from Laser Irradiation Experiments and Theoretical Spectral Simulations. *Icarus* 235: 187–206.

Neubeck, A., Duc, N. T., Hellevang, H., Oze, C., Bastviken, D., Bacsik, Z., and Holm, N. G. 2014. Olivine Alteration and H2 Production in Carbonate-Rich, Low Temperature Aqueous Environments. *Planetary and Space Science* 96: 51–61.

Noguchi, T., Nakamura, T., Kimura, M., Zolensky, M. E., Tanaka, M., Hashimoto, T., Konno, M., et al. 2011. Incipient Space Weathering Observed on the Surface of Itokawa Dust Particles. *Science* 333: 1121–25.

Pieters, C. M., and Noble, S. K. 2016. Space Weathering on Airless Bodies. *Journal of Geophysical Research: Planets* 121: 1865–84.

Rietmeijer, F. J. 1999. Metastable Non-stoichiometric Diopside and Mg-Wollastonite: An Occurrence in an Interplanetary Dust Particle. *American Mineralogist* 84: 1883–94.

Rietmeijer, F. J. M. 1991. Aqueous Alteration in Five Chondritic Porous Interplanetary Dust Particles. *Earth and Planetary Science Letters* 102: 148–157.

Rietmeijer, F. J. M. 2009. The Irradiation-Induced Olivine to Amorphous Pyroxene Transformation Preserved in an Interplanetary Dust Particle. *Astrophysics Journal* 705: 791–97.

Rodriguez-Navarro, C., Kudłacz, K., Cizer, Ö., and Ruiz-Agudo, E. 2015. Formation of Amorphous Calcium Carbonate and its Transformation into Mesostructured Calcite. *CrystEngComm* 17: 58–72.

Schwertmann, U. 1988. Goethite and Hematite Formation in the Presence of Clay Minerals and Gibbsite at 25 C. *Soil Science Society of America Journal* 52: 288–291.

Sharp, T. G., and DeCarli, P. S. 2006. Shock Effects in Meteorites. In *Meteorites and the Early Solar System II*, edited by D. S. Lauretta, and H. Y. McSween, Jr., vol. 943, 653–677. Tucson: University of Arizona Press.

Strazzulla, G., and Brunetto, R. 2017. Particle Accelerators as Tools to Investigate Astrochemistry. *Nuclear Physics News* 27: 23–27.

Strazzulla, G., Dotto, E., Binzel, R., Brunetto, R., Barucci, M. A., Blanco, A., and Orofino, V. 2005. Spectral Alteration of the Meteorite Epinal (H5) Induced by Heavy Ion Irradiation: A Simulation of Space Weathering Effects on near-Earth Asteroids. *Icarus* 174: 31–35.

Szalay, J. R., Poppe, A. R., Agarwal, J., Britt, D., Belskaya, I., Horányi, M., Nakamura, T., Sachse, M., and Spahn, F. 2018. Dust Phenomena Relating to Airless Bodies. *Space Science Reviews* 214: 1–47.

Thompson, M. S., Zega, T. J., Becerra, P., Keane, J. T., and Byrne, S. 2016. The Oxidation State of Nanophase Fe Particles in Lunar Soil: Implications for Space Weathering. *Meteoritics & Planetary Science* 51: 1082–95.

Van de Moortèle, B., Reynard, B., Rochette, P., Jackson, M., Beck, P., Gillet, P., McMillan, P. F., and McCammon, C. A. 2007. Shock-induced metallic iron nanoparticles in olivine-rich Martian meteorites. *Earth and Planetary Science Letters* 262: 37–49.

Wang, D., and Chen, M. 2006. Shock-Induced Melting, Recrystallization, and Exsolution in Plagioclase from the Martian Lherzolitic Shergottite GRV 99027. *Meteoritics & Planetary Science* 41: 519–527.

Weber, I., Böttger, U., Hanke, F., Reitze, M. P., Heeger, M., Adolphs, T., and Arlinghaus, H. F. 2022. Space Weathering Simulation of Micrometeorite Bombardment on Silicates and their Mixture for Space Application. *Journal of Raman Spectroscopy* 53: 411–19.

Weber, I., Böttger, U., Reitze, M. P., and Pavlov, S. 2023. Effects of Simulated Micrometeorite Bombardment of Rock-Forming Silicates in Raman spectra. *54th Lunar and Planetary Science Conference* (LPI Contribution no. 2806), abstract 1134.

Yang, Y., Zhang, H., Wang, Z., Yuan, Y., Li, S., Hsu, W., and Liu, C. 2016. Optical Spectroscopic Characterizations of Laser Irradiated Olivine Grains. *Astronomy and Astrophysics* 597: A50. https://doi.org/10.1051/0004-6361/201629327.

Zeng, X., Tang, H., Li, X., Zeng, X., Yu, W., Liu, J., and Zou, Y. 2021. Experimental Investigation of OH/H_2O in H+-Irradiated Plagioclase: Implications for the Thermal Stability of Water on the Lunar Surface. *Earth and Planetary Science Letters* 560: 116806.

Zhang, W., Liu, H., Zhou, Y., Liao, K., and Huang, Y. 2023. Effects of Neutron Irradiation on Densities and Elastic Properties of Aggregate-Forming Minerals in Concrete. *Nuclear Engineering and Technology* 55: 2147–57.

Zhu, K., Liu, J., Moynier, F., Qin, L., Alexander, C. M. O'D., Conel, M., and He, Y. 2019. Chromium Isotopic Evidence for an Early Formation of Chondrules from the Ornans CO Chondrite. *The Astrophysical Journal* 873: id. 82.

SUPPORTING INFORMATION

Additional supporting information may be found in the online version of this article.

Data S1. Raman spectra of minor components before and after the irradiations.

Table S1. Summary of observed minerals at different locations.

Table S2. Peaks and FWHM appeared before and after all of irradiations of olivine (a) for band 816 cm^{-1}. (b) Peaks and FWHM appeared after all of irradiation of olivine band 845 cm^{-1} (no. = measuring point ID at measuring area).

Table S3. Peaks and FWHM appeared after all of irradiation of pyroxene band 1010 cm^{-1} (no. = measuring point ID at measuring area). The Raman IDs are displayed at S7.

Table S4. Peaks and FWHM appeared after all of irradiation of feldspar band 509 (no. = measuring point ID at measuring area) Raman IDs are displayed at Fig. S7.

Table S5. FWHM values of silicates before and after irradiations.

Table S5a. FWHM values of silicates after the third irradiation course, Raman IDs are displayed at Figure S7.

Table S5b. FWHM values of silicates after the second irradiation course.

Table S5c. FWHM values of silicates after the first irradiation course.

Table S5d. FWHM values before irradiation.

Table S6a. Occurrence of minerals in Raman spectra before and after the irradiations.

Table S6b. Overview of mineral phases of all samples.